

Magnetic field dependence of the copper charge density wave order in a $\text{YBa}_2\text{Cu}_3\text{O}_7/\text{Nd}_{0.65}(\text{Ca}_{0.7}\text{Sr}_{0.3})_{0.35}\text{MnO}_3$ superlattice

R. Gaina^{1,2,*}, S. Sarkar^{1,*,‡}, M. Soulier¹, J. Khmaladze¹, E. Perret^{1,3}, A. Tcakaev⁴, V. Hinkov⁴, M. Bonura⁵, E. Weschke⁶, and C. Bernhard^{1,§}

¹Department of Physics and Fribourg Center for Nanomaterials, University of Fribourg, Chemin du Musée 3, CH-1700 Fribourg, Switzerland

²Laboratory for Neutron Scattering and Imaging, Paul Scherrer Institut, CH-5232 Villigen PSI, Switzerland

³Laboratory for Advanced Fibers, Empa, Swiss Federal Laboratories for Materials Science and Technology, Lerchenfeldstrasse 5, 9014 St. Gallen, Switzerland

⁴Experimentelle Physik IV and Würzburg-Dresden Cluster of Excellence *ct.qmat*, Fakultät für Physik und Astronomie, Universität Würzburg, Am Hubland, D-97074 Würzburg, Germany

⁵University of Geneva, Department of Quantum Matter Physics (DQMP), CH-1211 Geneva, Switzerland

⁶Helmholtz-Zentrum Berlin für Materialien und Energie, BESSY II, D-12489 Berlin, Germany



(Received 28 July 2021; revised 1 October 2021; accepted 15 October 2021; published 17 November 2021)

For a $\text{YBa}_2\text{Cu}_3\text{O}_7/\text{Nd}_{0.65}(\text{Ca}_{0.7}\text{Sr}_{0.3})_{0.35}\text{MnO}_3$ (YBCO/NCSMO) superlattice, we studied with resonant elastic x-ray scattering (REXS) at the Cu L_3 edge how the copper sublattice charge density wave (Cu-CDW) order in YBCO is affected by a large magnetic field up to 6.9 T that weakens the CE-type antiferromagnetic (AF) and the charge/orbital (Mn-CO) orders of the manganite in favor of a ferromagnetic state. While a field of only 2 T induces a strong ferromagnetic moment in the manganite, we find that the Bragg peak of the Cu-CDW hardly changes up to 6 T. Moreover, as the magnetic field is further increased to 6.9 T, the Cu-CDW Bragg peak gets suddenly enhanced and broadened, whereas the ferromagnetic moment of the manganite is already saturated. The observed uncorrelated magnetic field dependence of the charge orders in the cuprate and manganite layers suggests that these orders are not directly coupled across the interface. We rather interpret our data in terms of an indirect coupling via the domain boundaries of the Mn-CO and the related disorder and lattice strain. This interpretation is supported by additional studies of the magnetoelectric response, which provide evidence for a crossover in the dynamics of the Mn-CO in the range between 6 and 7 T, from a low-field state with pinned domains to a high-field state with more mobile and flexible domain boundaries. We attribute the concomitant enhancement and broadening of the Cu-CDW Bragg peak to this crossover.

DOI: [10.1103/PhysRevB.104.174513](https://doi.org/10.1103/PhysRevB.104.174513)

I. INTRODUCTION

The unusual normal state electronic properties of the cuprate high- T_c superconductors remain a subject of great interest. The parent compounds with a half-filled conduction band are antiferromagnetic (AFM) Mott-Hubbard insulators. Hole doping rapidly suppresses the Mott gap and the long-range AFM order and induces an anomalous conducting and even superconducting (SC) state of strongly correlated charge carriers [1,2]. The T_c value increases at first in the so-called underdoped regime, before it reaches a maximum around optimum doping of $p \approx 0.16$ and decreases again in the so-called overdoped regime, until it vanishes at $p > 0.33$ [3–5]. The corresponding normal state electronic properties are highly anomalous, especially in the underdoped regime where a partial gaplike depletion of the low-energy electronic states occurs already well above T_c [3,6,7]. The origin of

this so-called pseudogap phenomenon is still debated, with the explanations ranging from a precursor SC state that lacks macroscopic phase coherence [8] to various kinds of spin and/or charge orders that either compete directly with SC [9–11] or form more complex states for which the two orders are intertwined [12,13]. Initially, the research focus had been on short-ranged AFM spin correlations that persist in the strongly underdoped regime, where they coexist and compete with superconductivity. A prominent example is the so-called stripe order that becomes very pronounced in $\text{La}_{1-x}\text{Ba}_x\text{CuO}_4$ around $x = 1/8$ doping [14].

The more recent observation of an incommensurate Cu sublattice charge density wave (Cu-CDW) order in underdoped YBCO, first with nuclear magnetic resonance (NMR) [15] and subsequently with x-ray diffraction techniques [10,11], has renewed the interest in the relationship of competing orders with high- T_c superconductivity. The static Cu-CDW exists only in a limited doping range in the underdoped regime, where its onset temperature marks a dome-shaped curve with a maximum of $T^{\text{CDW}} \approx 150$ K around $p \approx 0.1$ [1,16]. In pristine YBCO crystals, the Cu-CDW is only short ranged, seems to be spatially inhomogeneous, and preferably nucleates in regions with enhanced disorder and around

*These authors contributed equally to this paper.

[†]roxana.gaina@unifr.ch

[‡]subhrangsu.sarkar@unifr.ch

[§]christian.bernhard@unifr.ch

defects [17,18]. The Bragg peak of this quasi-two-dimensional (2D) Cu-CDW order is rather broad, and its intensity tends to get suppressed below T_c due to a competition with superconductivity [10,11,16]. Nevertheless, signatures of dynamic charge density fluctuations are found for a much wider doping range within the phase diagram, including the overdoped regime, and for temperatures well above 150 K [19,20]. Moreover, it has been shown that external stimuli, such as a large magnetic field [21,22] or uniaxial strain [23], can induce a long-ranged and quasi-three-dimensional (3D) Cu-CDW order that is also correlated in the direction perpendicular to the CuO_2 planes.

An enhancement of the static Cu-CDW order was also observed in thin films of underdoped YBCO, for which a three-dimensional CDW order can develop in the absence of a large magnetic field or external strain [24]. It has been speculated that the interaction with the STO substrate helps to stabilize the Cu-CDW order in these thin films. Possible mechanisms range from an enhanced Fermi surface nesting due to the quasitragonal structure of the YBCO films with only short-ranged and strongly disordered CuO chain fragments, to a charge transfer and orbital hybridization [25] or phonon hybridization [26].

A quasi-2D Cu-CDW order has also been reported in superlattices of $\text{YBa}_2\text{Cu}_3\text{O}_7$ with the itinerant ferromagnetic manganite $\text{La}_{2/3}\text{Ca}_{1/3}\text{MnO}_3$ (LCMO) [27]. Even though the YBCO layers are fully oxygenated here, and thus nominally close to optimal doping, a broad Cu-CDW Bragg peak due to a quasi-2D Cu-CDW is below about 120 K. Likewise, it has been observed in YBCO/ $\text{Nd}_{0.65}(\text{Ca}_{1-y}\text{Sr}_y)_{0.35}\text{MnO}_3$ (YBCO/NCSMO) multilayers, for which the manganite is insulating and exhibits a CE-type AFM and charge/orbital order, with only a weak FM component [28]. Here it was shown that intensity of the Bragg peak of the quasi-2D Cu-CDW increases as the strength of the Mn-CO order is enhanced, via the Sr-content y , that determines the tolerance factor t , and thus the buckling of the Mn-O bonds and the related width of the conduction band. A very recent study of a YBCO/ $\text{Nd}_{0.5}(\text{Ca}_{1-y}\text{Sr}_y)_{0.5}\text{MnO}_3$ multilayer even found an entirely new kind of Cu-CDW order that seems to have a d_{z^2} rather than the usual $d_{x^2-y^2}$ orbital character and a rather small in-plane ordering wave vector of $Q_{\parallel} \approx 0.1$ reciprocal lattice units (r.l.u.) [29]. The higher-hole doping level of the manganite layers in these superlattices gives rise to a pure AF and a truly long-ranged Mn-CO order.

The findings described above call for further efforts to understand the intricate relationship between the charge and magnetic orders in these cuprate/manganite multilayers. Here we use resonant elastic x-ray scattering (REXS) at the Cu L_3 edge to study for a YBCO/NCSMO superlattice with $x = 0.35$ on how the Cu-CDW order is affected by a magnetic field up to 6.9 T, which is known to weaken the CE-type AF and Mn-CO orders and induce a strong FM moment.

II. EXPERIMENTAL DETAILS

A. Growth and characterization

A superlattice consisting of ten bilayers of 10 nm $\text{Nd}_{1-x}(\text{Ca}_{1-y}\text{Sr}_y)_x\text{MnO}_3$ (NCSMO with $x=0.35$ and $y=0.3$)

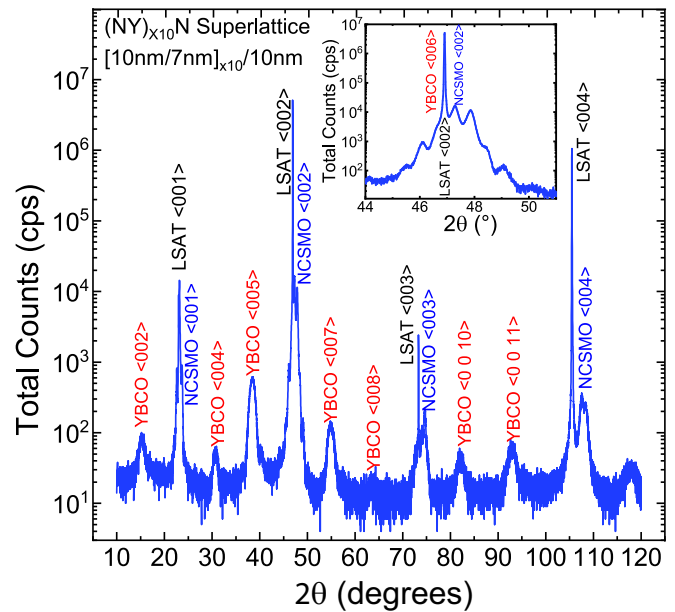


FIG. 1. X-ray diffraction curve (θ - 2θ scan) of the $\langle 00L \rangle$ peaks of the NCSMO/YBCO superlattice and the LSAT substrate that confirms its epitaxial growth and high structural quality. Inset: Magnification around the $\langle 002 \rangle$ and $\langle 006 \rangle$ peaks of NCSMO and YBCO, respectively, showing pronounced satellite peaks that testify for the high structural quality of the superlattice.

and 7 nm fully oxygenated $\text{YBa}_2\text{Cu}_3\text{O}_7$ (YBCO), with an additional 10 nm NCSMO layer on top, was epitaxially grown with pulsed laser deposition on a $\langle 001 \rangle$ -oriented $(\text{La}_{0.18}\text{Sr}_{0.82})(\text{Al}_{0.59}\text{Ta}_{0.41})\text{O}_3$ (LSAT) substrate. The excimer KrF laser $\lambda = 248$ nm, $T_s = 25$ ns had a beam-spot size on the target of 3 mm^2 , a repetition rate of 2 Hz, and a fluence of $\approx 1.42 \text{ J cm}^{-2}$. The LSAT substrate was glued with silver paint on a stainless-steel holder that was placed 5 cm above the targets and heated from the backside with an infrared laser at a rate of 10°C/min to a deposition temperature of 825°C . The deposition was performed at a pressure of 0.35 mbar of 99.5% pure oxygen gas. After the growth, the chamber was ventilated with pure oxygen gas to a about half atmospheric pressure, in which the sample was cooled to 480°C at a rate of 10°C/min . Subsequently, the sample was kept for about 1 h between 480 and 380°C to fully oxygenate the YBCO layers, before it was rapidly cooled to room temperature (by switching off the laser heater). The structural properties of the above-described superlattice have been determined with x-ray diffraction (XRD) using a Rigaku SmartLab 9 kW four-circle x-ray diffractometer with a rotating anode $\text{Cu-K}\alpha$ source.

A parallel incident parallel beam optics with a two-bounce Ge $\langle 220 \rangle$ monochromator ($\Delta\lambda/\lambda = 3.8 \times 10^{-4}$) has been used to extract the pure $\text{Cu-K}\alpha 1$ component. Figure 1 shows a so-called θ - 2θ scan of the $\langle 00L \rangle$ Bragg peaks of the YBCO/NCSMO superlattice and the LSAT substrate. The rather sharp and intense peaks of YBCO and NCSMO confirm the epitaxial growth and the high structural quality of the superlattice. The inset shows a magnified view of the most intense Bragg peak around $\langle 002 \rangle$ of NCSMO and $\langle 006 \rangle$ of YBCO which reveals a series of satellites that testify for the well-defined superlattice structure and the flatness and

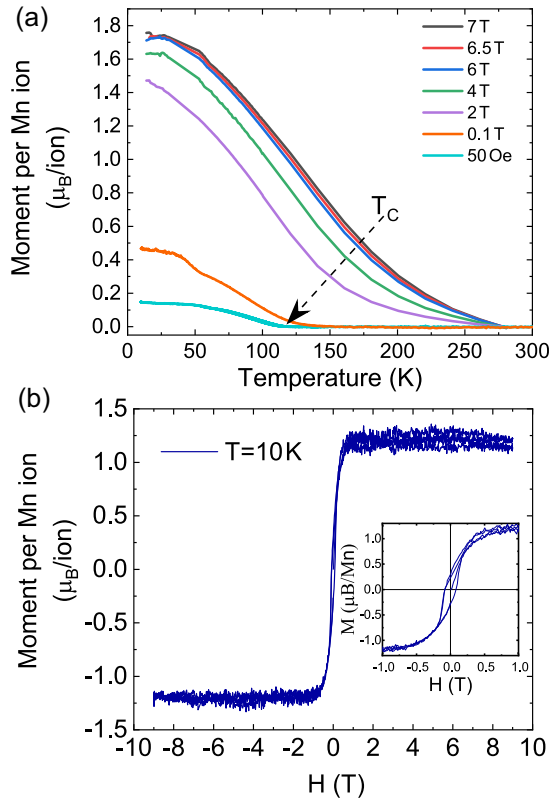


FIG. 2. (a) Temperature dependence of the DC magnetization in field-cooled mode with the magnetic field applied parallel to the layers of the superlattice. (b) Magnetization versus magnetic field loop at $T = 10$ K after zero-field cooling showing a ferromagnetic hysteresis. Note that the magnetization loop was obtained after zero-field cooling and has a smaller saturation moment than for the field-cooled magnetization in (a). Inset: Magnified view of the hysteresis curve around the origin.

sharpness of the interfaces. The obtained value of the c -axis parameter of the YBCO layers of 1.164 nm is consistent with a fully oxygenated state of the CuO chains.

B. Magnetization measurements

The magnetization of the superlattice was measured using a Quantum Design DC-SQUID magnetometer. The diamagnetic and paramagnetic signals from the LSAT substrate have been subtracted to obtain the magnetization from the superlattice. Figure 2(a) shows the magnetization versus temperature curves during field cooling with the magnetic field applied parallel to the layers of the superlattice. Note that in this configuration the diamagnetic screening of the superconducting YBCO layers is extremely weak, since the magnetic penetration depth along the c axis of YBCO is orders of magnitude larger than the layer thickness. The low-field magnetization curve at 50 Oe reveals the onset of a weak spontaneous magnetization below about 120 K with a low temperature value of the saturation moment of less than $0.2 \mu_B/\text{Mn ion}$. Note that the AFM order, which is expected to develop around 150 to 170 K, has a much weaker signal and is therefore not resolved. The ferromagnetic nature of the weak spontaneous magnetization signal is confirmed by the magnetization loop

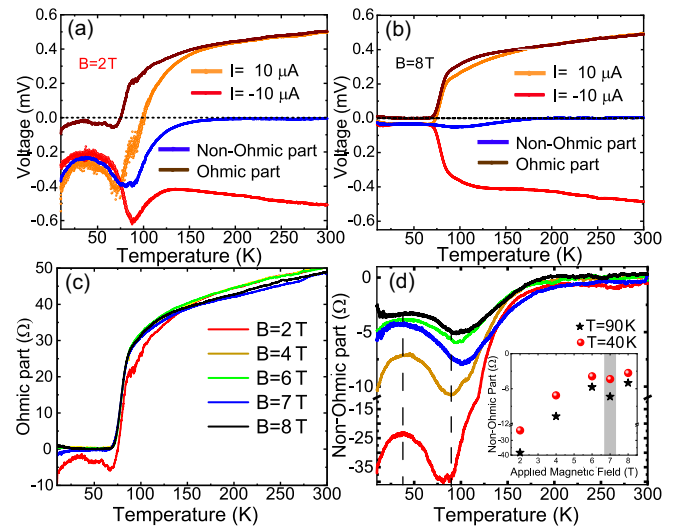


FIG. 3. Voltage vs temperature curves obtained in four-contact geometry with an applied current of $I = \pm 10 \mu\text{A}$ at (a) $B = 2$ T and (b) $B = 8$ T. The Ohmic and non-Ohmic signals have been obtained according to Eqs. (1) and (2). Temperature and magnetic field dependence of (c) the Ohmic signal and (d) the non-Ohmic signal. (Inset: Applied magnetic field dependence of the non-Ohmic signal at 40 and 90 K.)

(substrate contribution subtracted) in Fig. 2(b), which reveals a sizable hysteresis.

The origin of these ferromagnetic moments is not entirely clear yet. The interpretations range from a spin canting of the CE-type AFM state [30] to a phase segregated state with a mixture of FM and AFM domains. The saturation moment (or the fraction of the FM regions) increases quite rapidly to about $1.2 \mu_B/\text{Mn ion}$ as the magnetic field is raised to 2 T (see Fig. 2). Toward higher fields, this increase slows down, and the moment saturates at a value of about $1.75 \mu_B/\text{Mn ion}$ at 6 T (which corresponds to about 70% of the maximal value that is typically observed for 20-nm-thick layers of the ferromagnetic $\text{La}_{2/3}\text{Ca}_{1/3}\text{MnO}_3$ [31,32]). Notably, between 6 and 7 T there is hardly any further change of the saturation moment.

C. Measurements of magnetoelectric transport properties

Magnetotransport measurements have been performed with a physical property measurement system (PPMS) from Quantum Design equipped with a Keithley 2182a nanovoltmeter. Figures 3(a) and 3(b) show exemplary voltage versus temperature curves at 2 and 8 T, respectively. They were obtained in a four line-contact geometry with a current of $\pm 10 \mu\text{A}$ (orange and red) applied between the outer contacts, while the voltage across the inner contacts was recorded. At 2 T a pronounced asymmetry is evident between the curves at positive and negative currents. It is due to a spontaneous voltage that develops rather gradually below about 240 K, i.e., together with the Mn-CO, and increases more rapidly below about 100 K, where it reaches several tens of millivolts. This spontaneous voltage is largest at low field and arises most likely from a polar order due to the noncentrosymmetric Jahn-Teller distortions that accompany the Mn-CO and gives rise to

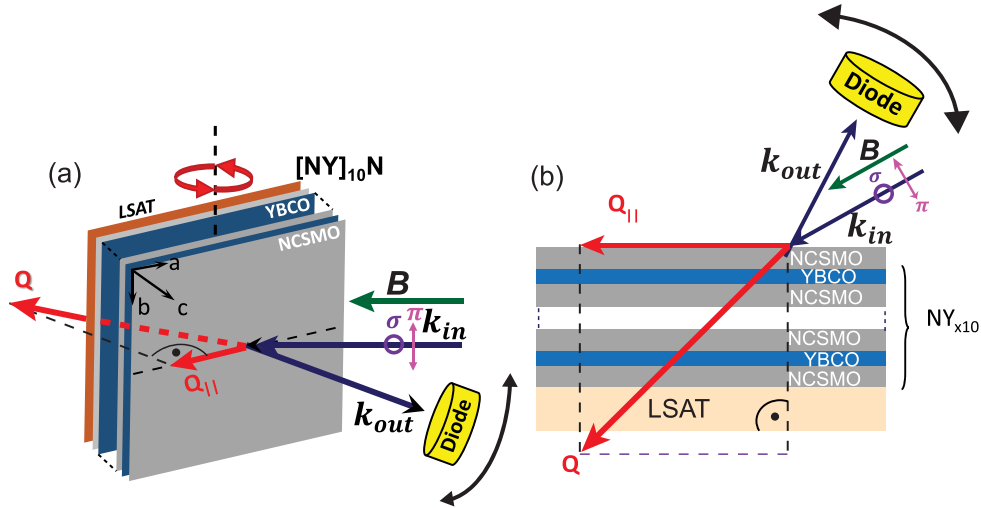


FIG. 4. Schematics of the YBCO/NCSMO superlattice and the configuration of the REXS experiment in grazing incidence geometry.

a domain state with frozen surface charges [33]. Figures 3(c) and 3(d) show the Ohmic and the non-Ohmic parts of the signal, respectively, that have been obtained according to

$$\text{Ohmic part} = \frac{V^+}{I^+} + \frac{V^-}{I^-} = R_0, \quad (1)$$

$$\text{Non-Ohmic part} = \frac{V^+}{I^+} - R_0. \quad (2)$$

The non-Ohmic signal gets strongly suppressed by the magnetic field, but a weak signal persists even at a field as high as 8 T. At $B > 4$ T, the corresponding Ohmic signal exhibits the expected metallic response of the YBCO layers, with a superconducting transition that has an onset around 85 K and is completed below 70 K. At 2 T (and below), the Ohmic curve is strongly distorted, indicating that the voltage contributions due to the applied current and the frozen surface charges cannot be readily separated anymore. A discussion of the complex magnetoelectronic response in this low-field regime is beyond the scope of this paper and is referred to a separate publication.

D. Measurement of the Cu-CDW by REXS

The REXS experiments were performed at the UE46-PGM1 beamline of the BESSY II synchrotron in Berlin, Germany. The sample was mounted at first in the XUV diffractometer, where it was pre-aligned and wide range scans were performed to determine the position of the Cu-CDW Bragg peak and the shape of the background around it. Subsequently, the superlattice was transferred to the ultrahigh vacuum high-field diffractometer setup, where the scanning range was restricted to a narrow range around the Cu-CDW Bragg peak.

Figure 4 shows sketches of the superlattice and the scattering geometry of the REXS setup for which the magnetic field is applied parallel to the incident x-ray beam. The energy of the incident x-ray photons with wave vector \mathbf{k}_{in} was set to the maximum of the resonance at the Cu L_3 edge that was determined from the XAS measurements in total fluorescence yield mode measurement.

The incident beam had a spot size of about $2 \text{ mm} \times 1.5 \text{ mm}$ ($H \times V$) and was linearly polarized in σ configuration. The scattered x rays with wave vector \mathbf{k}_{out} were detected with a photodiode that could be moved along 2θ and the z direction. Scans of the scattering vector $\mathbf{Q} = \mathbf{k}_{\text{in}} - \mathbf{k}_{\text{out}}$ were performed by rotating the vertically mounted sample along θ and a concomitant 2θ movement of the detector. In the zero field XUV diffractometer, the scans along the H component of the scattering vector (in the sketch denoted as $Q_{\parallel} \approx 0.1$) were performed with K kept constant at 0, while L was also kept constant at ≈ 1.45 in units of the reciprocal lattice units (r.l.u.) of the YBCO unit cell. In the high magnetic field diffractometer, only the sample angle (θ) was changed, whereas the position of the detector was kept constant such that H and L were scanned simultaneously between $-0.463 < H < -0.138$ and $1.0 < L < 1.67$ with $L = 1.43$ at the position of the CDW peak. The latter parameters were chosen to match the ones of a previous RIXS experiment on a similar multilayer, for which the maximum of the Bragg peak of the quasi-2D Cu-CDW was measured around $(H, K, L) = (-0.33, 0, 1.45)$. In this latter experiment it was also shown that the Bragg peak of the quasi-2D Cu-CDW exhibits a pronounced resonance around 931 eV that nearly coincides with the maximum of the x-ray absorption signal in fluorescence-yield mode [28], confirming that the Cu-CDW originates from the CuO_2 planes of YBCO and not from the CuO chains (for which a resonance around 933.8 eV would be expected [34]). Measurements in the XUV diffraction chamber were performed in both grazing incidence (GI, $\theta_{\text{in}} < \theta_{\text{out}}$) and grazing exit (GE, $\theta_{\text{in}} > \theta_{\text{out}}$), geometries, as shown in Fig. 5.

In the high magnetic field diffractometer, due to geometric restrictions, the measurements were only performed in GI geometry. Here the magnetic field was at an angle of 46.026° with respect to the surface normal at the position of the Bragg peak of the Cu-CDW order.

Figures 5(a) and 5(b) display representative REXS diffraction curves across the Cu-CDW Bragg peak of the YBCO layers in grazing incidence (GI, $Q_{\parallel} < 0$) and grazing exit (GE, $Q_{\parallel} > 0$) geometry, that were obtained with the XUV diffractometer at the maximum of the Cu L_3 -edge reso-

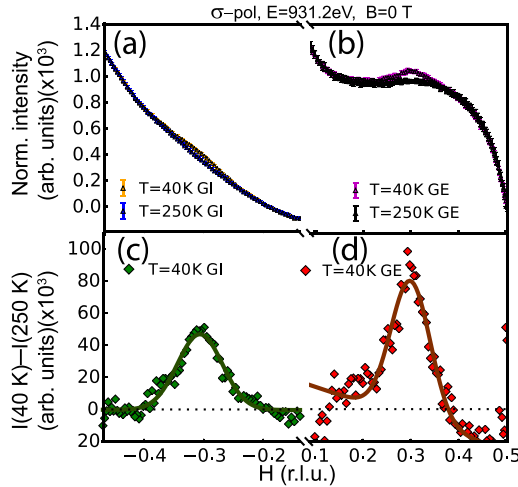


FIG. 5. (a) and (b) Normalized diffraction curves around the Bragg peak of the Cu-CDW of YBCO measured in GI geometry (left panel) and GE geometry (right panel) near the maximum of the Cu L_3 -edge resonance (931 eV) at $B = 0$ T and temperatures of 40 and 250 K. (c) and (d) Bragg peak of the Cu-CDW after subtracting the curve at 250 K, which represents the background signal. Solid lines show the best fits with a Gaussian function.

nance (931 eV). The curves have been normalized in the Q ranges well below and above the Bragg peak, as described in the experimental section. A clear Bragg peak around $H \approx \pm 0.3$ r.l.u. is evident here in the GI and GE curves at 40 K and is absent (or at least much weaker and/or broader) in the corresponding curves at 250 K.

We would like to remind that the YBCO layers in our superlattice have a thickness of only 7 nm (or about 6 unit cells), yet the superconducting transition has an onset around 85 K and is complete below 70 K. The fact that the Cu-CDW peak position at lowest temperature and $B = 0$ T is $H = -0.305$ r.l.u., indicates a near-optimal doping level [27].

In the following analysis we have therefore used the 250 K curve as background and have subtracted it from the curves at lower temperatures as to determine the signal of the Bragg peak due to the Cu-CDW. Figures 5(c) and 5(d) show the corresponding difference plots between the curves at 40 and 250 K (symbols) together with a Gaussian fit of the Bragg peak (solid curves). They confirm that the Cu-CDW Bragg peak shows up in both the GI and GE geometries. They also reveal that the 250 K curve has a simpler shape and the background subtraction is thus more reliable for the GI geometry than for the GE geometry. Accordingly, the following study of the temperature and magnetic field dependence of the Cu-CDW Bragg peak has been performed in GI geometry.

Figure 6 shows the diffraction curves in GI geometry (left-hand panels) and the difference plots with respect to the curves at 250 K (right-hand panels) at selected temperatures (colored symbols) in magnetic fields of $B = 0$ T in Figs. 6(a) and 6(b), 6 T in Figs. 6(c) and 6(d), and 6.9 T in Figs. 6(e) and 6(f).

The solid lines in the right-hand panels show the corresponding Gaussian fits of the Cu-CDW Bragg peak in the temperature difference plots.

At zero magnetic field, the Bragg peak is strongest at 6 K and its peak area decreases continuously towards higher temperature, without a clear anomaly around $T_c \approx 80$ K. The Bragg peak finally vanishes somewhat above 150 K, in good agreement with the result of previous RIXS studies of a corresponding NYN trilayer with $x = 0.35$ and $y = 0.2$ with an onset temperature of the Cu-CDW order around 175 K [28]. The low temperature value of the in-plane wave vector of the present superlattice with $x = 0.35$ and $y = 0.3$ of $Q_{\parallel} \approx -0.31$ r.l.u. is slightly lower than for the NYN trilayer with $x = 0.35$ and $y = 0.2$ with $Q_{\parallel} \approx -0.34$ r.l.u. The peak width of the present multilayer with $\Delta Q_{\parallel} \approx 0.07$ r.l.u. is about four times larger than the one reported for the NYN trilayer with $x = 0.35$ and $y = 0.2$. Note, however, that the Cu-CDW wave vector in these heterostructures may exhibit a lateral variation and the measured peak width can thus depend on the size of the footprint of the incident x-ray beam [29]. The spot size of the present high-field REXS setup of about $2\text{ mm} \times 1.5\text{ mm}$ ($H \times V$) is indeed larger than the one of the RIXS setup of $52\text{ }\mu\text{m} \times 4\text{ }\mu\text{m}$ ($H \times V$) used in Ref. [35].

Next, we discuss how the Cu-CDW Bragg peak changes in response to an applied magnetic field. Figure 7 reveals that up to 6 T the magnetic field does not have a noticeable effect on the Cu-CDW Bragg peak, i.e., the peak area [Fig. 7(a)], peak position [Fig. 7(b)], and peak width [Fig. 7(d)] remain constant within the error bars.

This result is rather surprising since this magnetic field has a strong effect on the electronic and magnetic properties of the manganite layers, for which it strongly suppresses the AFM and Mn-CO orders and induces instead a ferromagnetic order instead.

Equally surprising is our observation that the Bragg peak suddenly gets enhanced as the magnetic field is further increased from 6 to 6.9 T. Figure 7(a) shows that the Bragg-peak area (or intensity) at 10 K is nearly doubled at 6.9 T as compared to the value at 6 T. The comparison with Figs. 7(c) and 7(d) reveals that the growth of the peak area arises from a concomitant increase of the amplitude and the width of the Bragg peak. Moreover, Fig. 7(a) shows that this enhancement of the Cu-CDW between 6 and 6.9 T develops only below 120 K and does not show a clear anomaly at the SC transition of $T_c \approx 80$ K [see Fig. 7(a)]. Since the magnetic field of the REXS setup is limited to 6.9 T, we could unfortunately not explore whether the Cu-CDW Bragg peak exhibits further changes at higher magnetic fields.

Before discussing the implications of this unusual magnetic field dependence of the Cu-CDW with respect to its relationship with the magnetic and charge orders in the manganite layers, we present in Sec. II E additional pertinent aspects of the magnetoelectric response. In particular, we discuss some anomalous changes of the magnetoelectric response, which occur in the range between 6 and 7 T and thus seem to be related to the concomitant enhancement and broadening of the Cu-CDW Bragg peak.

E. Temperature and magnetic field dependence of the spontaneous voltage at zero bias

The magnetoelectric response of the superlattice exhibits anomalies in the range between 6 and 7 T, which indicate that

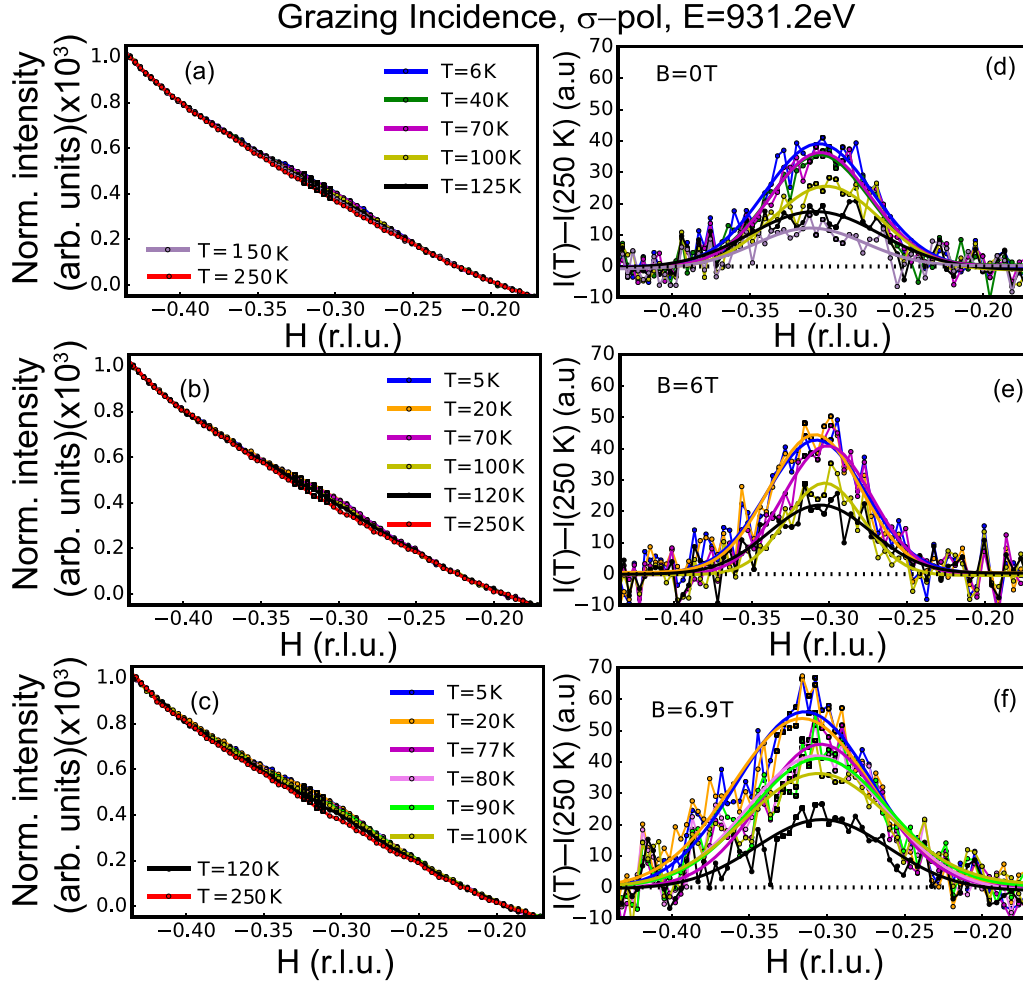


FIG. 6. (a) and (d), (b) and (e), and (c) and (f) Demonstrate the temperature dependence of the normalized diffraction curves around the Bragg peak of the Cu-CDW of YBCO measured in grazing incidence (GI) geometry and the corresponding background subtracted Bragg peaks of the Cu-CDW obtained by subtracting the curves from those at 250 K as background signal at 0, 6, and 6.9 T, respectively. Solid lines show Gaussian fits of the Bragg peak.

the Mn-CO undergoes changes from a low-field state with frozen domains to a high-field state with more mobile and flexible domain boundaries. Figure 3(d) shows that the non-Ohmic response, which is overall strongly suppressed by the magnetic field, exhibits an anomalous enhancement around 7 T. Likewise, the magnetic field loop of the spontaneous voltage at 30 K in Fig. 8(a) reveals a crossover from an irreversible to a reversible behavior of the magnetoelectric response in the range between 6 and 7 T (gray shaded area) that signifies a corresponding change in the dynamics of the Mn-CO domain state. The magnetic field loop at 90 K in Fig. 8(b) also exhibits a pronounced anomaly due to an abrupt change of the slope between 6 and 7 T. Finally, Fig. 8(c) confirms that these anomalies are absent in the field loop at 150 K, for which the spontaneous voltage evolves continuously and reversibly in the entire measured magnetic field range. A detailed discussion of this multiferroic behavior, which is also observed in NCSMO single layers, will be presented in a separate paper.

Here we only emphasize and discuss the anomalous changes in the range between 6 and 7 T that are suggestive of a crossover in the dynamics of the Mn-CO domain state

that coincides with the enhancement and broadening of the Cu-CDW Bragg peak that has been observed in our REXS study, as shown in Fig. 7.

III. DISCUSSION

Our Cu L_3 -edge REXS study reveals that the Bragg peak of the Cu-CDW of YBCO is hardly affected by a magnetic field up to 6 T, whereas it gets strongly enhanced and broadened as the field is further increased to 6.9 T. This magnetic field dependence of the Cu-CDW is remarkably unrelated to the one of the AFM and Mn-CO orders of the manganite, which get strongly suppressed by the magnetic field at a rate that is largest between 0 and 4 T and saturates between 6 and 7 T. The latter behavior is evident from the dc magnetization data in Fig. 2(a) and the magnetotransport data in Fig. 3. It also agrees with the previously reported behavior of manganite single crystals [30] and thin films [36,37] with similar hole doping of $x = 0.3\text{--}0.35$ and tolerance factor of $t \approx 0.95$. Here a magnetic field of a few Tesla suppresses the CE-type AFM and the combined charge and $d_{3x^2-r^2}$ type orbital orders and induces a ferromagnetic state.

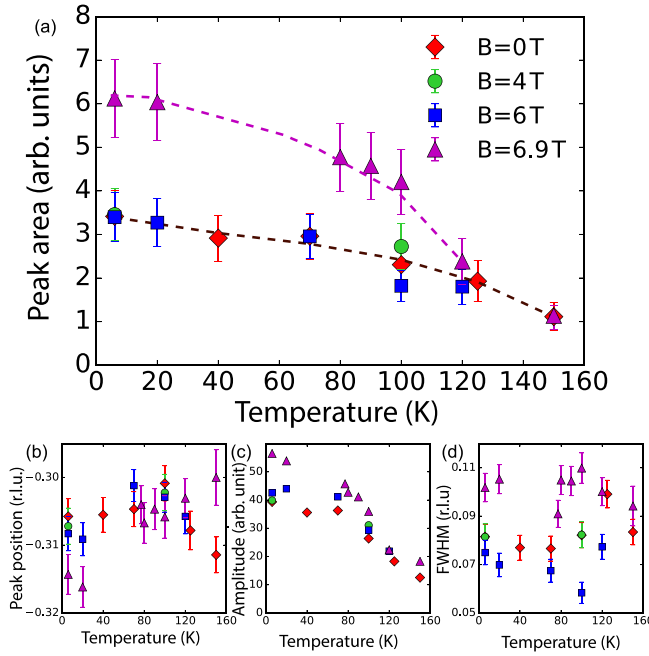


FIG. 7. Temperature and magnetic field dependence of the Bragg peak due to the Cu-CDW of the YBCO layers. The parameters obtained with Gaussian fits are displayed for (a) the area, (b) the position, (c) the height, and (d) the full-width at half-maximum (FWHM) of the peak at fields of 0 (red), 4 (green), 6 (blue), and 6.9 T (violet). The dashed lines in (a) are guides to the eye.

The above described observations lead us to our main conclusion that there seems to be no direct coupling between the order parameters of the Cu-CDW of YBCO and the AF and Mn-CO of the manganite layers, neither a constructive nor a destructive one. Note that there exists also no evidence that the ferromagnetic order, which is strongly enhanced by the external magnetic field, suppresses superconductivity (via an interfacial exchange interaction with the spin-singlet Cooper pairs) and thus strengthens the competing Cu-CDW. Figure 2 shows indeed that the ferromagnetic moment saturates in the range between 6 and 7 T where the Bragg peak of the Cu-CDW is anomalously enhanced. Moreover, the Ohmic part of the magnetoelectric response in Fig. 3(c) shows no clear sign of a suppression of the SC transition by the magnetic field and the induced FM moment. This excludes an analogous interpretation of the magnetic field induced enhancement of the Cu-CDW as in strongly underdoped YBCO single crystals, for which the magnetic field strongly suppresses the competing superconducting order [21]. Likewise, for the present superlattice, the temperature dependence of the Cu-CDW Bragg peak in zero magnetic field shows no sign of a suppression below T_c and thus of a competition of the Cu-CDW with superconductivity. Note that such a lack of a direct competition between the Cu-CDW and superconductivity was previously reported from a REXS study on related YBCO/La_{2/3}Ca_{1/3}MnO₃ (YBCO/LCMO) multilayers for which the intensity of the Cu CDW peak also showed no sign of a suppression below T_c nor did it change in magnetic fields up to 6 T [27]. Moreover, in this previous REXS study it was shown that the intensity of the Cu-CDW

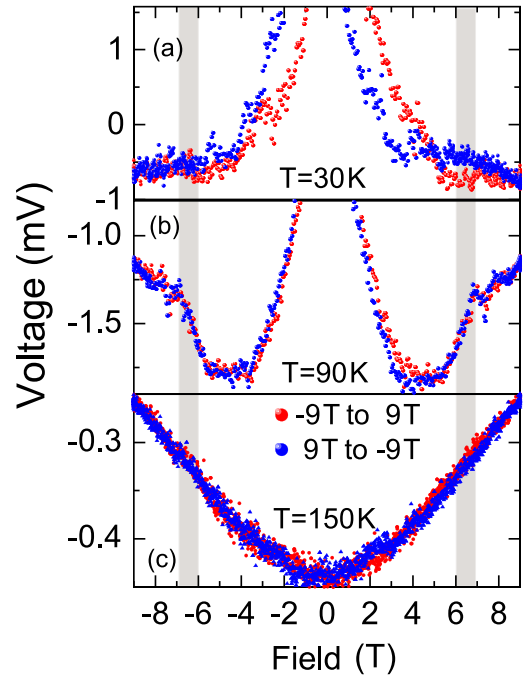


FIG. 8. Magnetic field loops of the spontaneous voltage that develops between two silver contacts on the topmost NCSMO layer without an applied current at temperatures of (a) 30, (b) 90, and (c) 150 K. Gray bars mark the region between 6 and 7 T.

Bragg peak increases with the thickness of the YBCO layers (that was varied between 10 and 50 nm). This provides strong evidence that in these YBCO/manganite multilayers the quasi-2D Cu-CDW is bulklike phenomenon which is not limited to the CuO₂ planes right at the interface that tend to be strongly underdoped, due to the charge (hole) transfer across the cuprate/manganite interface [25,27,38,39].

In the following we therefore discuss the scenario of an indirect coupling for which the domain boundaries of the AF and Mn-CO orders of the manganite layers act as nucleation centers for the formation of a Cu-CDW order in the adjacent YBCO layers. The strain and disorder in the vicinity of these domain boundaries can locally suppress (or strongly weaken) the superconductivity in the adjacent YBCO layers and thus favor the formation of the Cu-CDW. Accordingly, the latter would be spatially inhomogeneous and exhibit a networklike structure similar to the one of the Mn-CO domain boundaries. Such a scenario can explain why in these YBCO/manganite multilayers there is no competition between the Cu-CDW and superconductivity. Moreover, it can account for the rather large width of the Cu-CDW Bragg peak and, in particular, for the concomitant enhancement and broadening of the Cu-CDW Bragg peak as the field is increased from 6 to 6.9 T. The magnetoelectric response in Fig. 3(d) and Figs. 8(a) and 8(b) reveal indeed some characteristic anomalies in the range between 6 and 7 T, which indicate that the Mn-CO undergoes a crossover from a low-field state with frozen domain boundaries to a high-field state, for which the domain boundaries are mobile. In the latter high-field state, the domain boundaries of the Mn-CO thus might be more abundant and flexible such that they can better adapt to structures

and defects that are favorable for the Cu-CDW order in the adjacent YBCO layers. The simultaneous enhancement and broadening of the Cu-CDW Bragg peak between 6 and 7 T thus can be understood in terms of the more abundant and randomly distributed domain boundaries of the Mn-CO in the high-field regime. In this context we also mention the work of Bluschke *et al.* [40] which demonstrates a disorder induced modification of the correlation length of the Cu-CDW in $(\text{Ca}_x\text{La}_{1-x})(\text{Ba}_{1.75-x}\text{La}_{0.25+x})\text{Cu}_3\text{O}_y$ single crystals. In their case, the disorder arises primarily from the random distribution of cations with different charges and ionic radii.

Clearly more work will be needed to obtain a better understanding of the complex relationship between the various charge and spin superconducting orders in such oxide-based heterostructures and the influence of disorder and extended defects such as the domain boundaries that may originate from adjacent layers.

IV. CONCLUSION

In summary, the presented data reveal a rather complex behavior concerning the relationship between the charge orders in the cuprate and manganite layers and their interplay with high temperature superconductivity. An important role seems to be played by the domain boundaries of the Mn-CO and their abundancy and flexibility, which implies that the Cu-CDW might be spatially inhomogeneous and develop preferably in regions where the SC order parameter is weakened or even suppressed. Scanning probe experiments could confirm such a spatially inhomogeneous distribution of the superconducting and Cu-CDW orders and thus shed more light on this

issue. Open questions also exist concerning the role of the antiferromagnetic and the subordinate ferroelectric orders that accompany the Mn-CO. The interplay between these various magnetic and charge orders is far from being understood and needs to be further investigated experimentally and theoretically. Ultimately, a better understanding of the resulting complex quantum states may be useful for the design of next generation quantum devices with multiple control variables and new functionalities.

ACKNOWLEDGMENTS

We acknowledge Dr. Stefano Gariglio from the University of Geneva, for allowing us access to the Quantum Design SQUID VSM at DQMP, University of Geneva. We also thank Mr. Jonas Knobel for his help with LaTeX compilations. We thank Helmholtz-Zentrum, Berlin (HZB) for financial support and the allocation of synchrotron radiation beamtime at the UE46_PGM-1 beamline at the BESSY II synchrotron. This project received funding from the European Union's Horizon 2020 research and innovation program under Grant Agreement No. 730872. Work at the University of Fribourg was supported by the Swiss National Science Foundation (SNSF) through Grants No. 200020-172611 and No. CRSII2-154410/1. Work at the University of Würzburg was supported by the Deutsche Forschungsgemeinschaft (DFG, German Research Foundation) - project-ID 258499086 - SFB 1170 (proj. C06) and the Würzburg-Dresden Cluster of Excellence on Complexity and Topology in Quantum Matter ct.qmat (EXC 2147, Project No. 390858490). We acknowledge V. Zabolotnyy for useful discussions.

-
- [1] B. Keimer, S. A. Kivelson, M. R. Norman, S. Uchida, and J. Zaanen, *Nature (London)* **518**, 179 (2015).
 - [2] P. A. Lee, N. Nagaosa, and X.-G. Wen, *Rev. Mod. Phys.* **78**, 17 (2006).
 - [3] H. Alloul, T. Ohno, and P. Mendels, *Phys. Rev. Lett.* **63**, 1700 (1989).
 - [4] J. W. Loram, K. A. Mirza, J. R. Cooper, and W. Y. Liang, *Phys. Rev. Lett.* **71**, 1740 (1993).
 - [5] S. Hüfner, M. A. Hossain, A. Damascelli, and G. A. Sawatzky, *Rep. Prog. Phys.* **71**, 062501 (2008).
 - [6] C. C. Homes, T. Timusk, R. Liang, D. A. Bonn, and W. N. Hardy, *Phys. Rev. Lett.* **71**, 1645 (1993).
 - [7] L. Yu, D. Munzar, A. V. Boris, P. Yordanov, J. Chaloupka, T. Wolf, C. T. Lin, B. Keimer, and C. Bernhard, *Phys. Rev. Lett.* **100**, 177004 (2008).
 - [8] V. J. Emery and S. A. Kivelson, *Nature (London)* **374**, 434 (1995).
 - [9] J. M. Tranquada, J. D. Axe, N. Ichikawa, A. R. Moodenbaugh, Y. Nakamura, and S. Uchida, *Phys. Rev. Lett.* **78**, 338 (1997).
 - [10] G. Ghiringhelli, M. Le Tacon, M. Minola, S. Blanco-Canosa, G. Mazzoli, N. B. Brookes, G. M. De Luca, A. Frano, D. G. Hawthorn, F. He, T. Loew, M. M. Sala, D. C. Peets, M. Salluzzo, E. Schierle, R. Sutarto, G. A. Sawatzky, E. Weschke, B. Keimer, and L. Braicovich, *Science* **337**, 821 (2012).
 - [11] J. Chang, E. Blackburn, A. T. Holmes, N. B. Christensen, J. Larsen, J. Mesot, R. Liang, D. A. Bonn, W. N. Hardy, A. Watenphul, M. v. Zimmermann, E. M. Forgan, and S. M. Hayden, *Nat. Phys.* **8**, 871 (2012).
 - [12] E. Fradkin, S. A. Kivelson, and J. M. Tranquada, *Rev. Mod. Phys.* **87**, 457 (2015).
 - [13] S. D. Edkins, A. Kostin, K. Fujita, A. P. Mackenzie, H. Eisaki, S. Uchida, S. Sachdev, M. J. Lawler, E.-A. Kim, J. C. Séamus Davis, and M. H. Hamidian, *Science* **364**, 976 (2019).
 - [14] J. M. Tranquada, B. J. Sternlieb, J. D. Axe, Y. Nakamura, and S. Uchida, *Nature (London)* **375**, 561 (1995).
 - [15] T. Wu, H. Mayaffre, S. Krämer, M. Horvatić, C. Berthier, W. N. Hardy, R. Liang, D. A. Bonn, and M. H. Julien, *Nature (London)* **477**, 191 (2011).
 - [16] S. Blanco-Canosa, A. Frano, E. Schierle, J. Porras, T. Loew, M. Minola, M. Bluschke, E. Weschke, B. Keimer, and M. Le Tacon, *Phys. Rev. B* **90**, 054513 (2014).
 - [17] M. L. Tacon, A. Bosak, S. M. Souliou, G. Dellea, T. Loew, R. Heid, K.-P. Bohnen, G. Ghiringhelli, M. Krisch, and B. Keimer, *Nat. Phys.* **10**, 52 (2014).
 - [18] T. Wu, H. Mayaffre, S. Krämer, M. Horvatić, C. Berthier, W. Hardy, R. Liang, D. Bonn, and M.-H. Julien, *Nat. Commun.* **6**, 6438 (2015).
 - [19] R. Arpaia, S. Caprara, R. Fumagalli, G. De Vecchi, Y. Y. Peng, E. Andersson, D. Betto, G. M. De Luca, N. B. Brookes, F. Lombardi, M. Salluzzo, L. Braicovich, C. Di Castro, M. Grilli, and G. Ghiringhelli, *Science* **365**, 906 (2019).

- [20] R. Arpaia and G. Ghiringhelli, *J. Phys. Soc. Jpn.* **90**, 111005 (2021).
- [21] S. Gerber, H. Jang, H. Nojiri, S. Matsuzawa, H. Yasumura, D. A. Bonn, R. Liang, W. N. Hardy, Z. Islam, A. Mehta, S. Song, M. Sikorski, D. Stefanescu, Y. Feng, S. A. Kivelson, T. P. Devereaux, Z. X. Shen, C. C. Kao, W. S. Lee, D. Zhu *et al.*, *Science* **350**, 949 (2015).
- [22] J. Chang, E. Blackburn, O. Ivashko, A. T. Holmes, N. B. Christensen, M. Hücker, R. Liang, D. A. Bonn, W. N. Hardy, U. Rütt, M. V. Zimmermann, E. M. Forgan, and S. M. Hayden, *Nat. Commun.* **7**, 11494 (2016).
- [23] H. H. Kim, S. M. Souliou, M. E. Barber, E. Lefrançois, M. Minola, M. Tortora, R. Heid, N. Nandi, R. A. Borzi, G. Garbarino, A. Bosak, J. Porras, T. Loew, M. König, P. M. Moll, A. P. Mackenzie, B. Keimer, C. W. Hicks, and M. Le Tacon, *Science* **362**, 1040 (2018).
- [24] M. Bluschke, A. Frano, E. Schierle, D. Putzky, F. Ghorbani, R. Ortiz, H. Suzuki, G. Christiani, G. Logvenov, E. Weschke, R. J. Birgeneau, E. H. da Silva Neto, M. Minola, S. Blanco-Canosa, and B. Keimer, *Nat. Commun.* **9**, 2978 (2018).
- [25] J. Chakhalian, J. W. Freeland, H. Habermeier, G. Cristiani, G. Khaliullin, M. V. Veenendaal, and B. Keimer, *Science* **318**, 1114 (2007).
- [26] N. Driza, S. Blanco-Canosa, M. Bakr, S. Soltan, M. Khalid, L. Mustafa, K. Kawashima, G. Christiani, H. U. Habermeier, G. Khaliullin, C. Ulrich, M. Le Tacon, and B. Keimer, *Nat. Mater.* **11**, 675 (2012).
- [27] A. Frano, S. Blanco-Canosa, E. Schierle, Y. Lu, M. Wu, M. Bluschke, M. Minola, G. Christiani, H. U. Habermeier, G. Logvenov, Y. Wang, P. A. Van Aken, E. Benckiser, E. Weschke, M. Le Tacon, and B. Keimer, *Nat. Mater.* **15**, 831 (2016).
- [28] E. Perret, C. Monney, S. Johnston, J. Khmaladze, F. Lyzwa, R. Gaina, M. Dantz, J. Pellicciari, C. Piamonteze, B. P. P. Mallett, M. Minola, B. Keimer, T. Schmitt, and C. Bernhard, *Commun. Phys.* **1**, 45 (2018).
- [29] R. Gaina, C. W. Nicholson, M. Rumo, S. Sarkar, J. Khmaladze, E. Paris, Y. Tseng, W. Zhang, T. C. Asmara, D. McNally, C. Piamonteze, E. Weschke, T. Schmitt, C. Monney, and C. Bernhard, *npj Quantum Mater.* **6**, 12 (2021).
- [30] Y. Tokura, *Rep. Prog. Phys.* **69**, 797 (2006).
- [31] S. Valencia, L. Balcells, B. Martínez, and J. Fontcuberta, *J. Appl. Phys.* **93**, 8059 (2003).
- [32] D. K. Satapathy, M. A. Uribe-Laverde, I. Marozau, V. K. Malik, S. Das, T. Wagner, C. Marcelot, J. Stahn, S. Brück, A. Rühm, S. Macke, T. Tietze, E. Goering, A. Frañó, J. H. Kim, M. Wu, E. Benckiser, B. Keimer, A. Devishvili, B. P. Toperverg *et al.*, *Phys. Rev. Lett.* **108**, 197201 (2012).
- [33] C. Jooss, L. Wu, T. Beetz, R. F. Klie, M. Beleggia, M. A. Schofield, S. Schramm, J. Hoffmann, and Y. Zhu, *Proc. Natl. Acad. Sci. USA* **104**, 13597 (2007).
- [34] A. J. Achkar, R. Sutarto, X. Mao, F. He, A. Frano, S. Blanco-Canosa, M. LeTacon, G. Ghiringhelli, L. Braicovich, M. Minola, M. Moretti Sala, C. Mazzoli, R. Liang, D. A. Bonn, W. N. Hardy, B. Keimer, G. A. Sawatzky, and D. G. Hawthorn, *Phys. Rev. Lett.* **109**, 167001 (2012).
- [35] V. N. Strocov, T. Schmitt, U. Flechsig, T. Schmidt, A. Imhof, Q. Chen, J. Raabe, R. Betemps, D. Zimoch, J. Krempasky, X. Wang, M. Grioni, A. Piazzalunga, and L. Patthey, *J. Synchrotron Radiat.* **17**, 631 (2010).
- [36] B. P. P. Mallett, J. Khmaladze, P. Marsik, E. Perret, A. Cerreta, M. Orlita, N. Biškup, M. Varela, and C. Bernhard, *Phys. Rev. B* **94**, 180503(R) (2016).
- [37] J. Khmaladze, S. Sarkar, M. Soulier, F. Lyzwa, R. de Andres Prada, E. Perret, B. P. P. Mallett, M. Minola, B. Keimer, and C. Bernhard, *Phys. Rev. Mater.* **3**, 084801 (2019).
- [38] J. Chakhalian, J. W. Freeland, G. Srajer, J. Stremper, G. Khaliullin, J. C. Cezar, T. Charlton, R. Dalgliesh, C. Bernhard, G. Cristiani, H.-U. Habermeier, and B. Keimer, *Nat. Phys.* **2**, 244 (2006).
- [39] K. Sen, E. Perret, A. Alberca, M. A. Uribe-Laverde, I. Marozau, M. Yazdi-Rizi, B. P. P. Mallett, P. Marsik, C. Piamonteze, Y. Khaydukov, M. Döbeli, T. Keller, N. Biškup, M. Varela, J. Vašátko, D. Munzar, and C. Bernhard, *Phys. Rev. B* **93**, 205131 (2016).
- [40] M. Bluschke, M. Yaari, E. Schierle, G. Bazalitsky, J. Werner, E. Weschke, and A. Keren, *Phys. Rev. B* **100**, 035129 (2019).